

Article

Two-Stage Late Jurassic to Early Cretaceous Hydrothermal Activity in the Sakar Unit of Southeastern Bulgaria

Krzysztof Szopa ^{1,*} , Anna Sałacińska ², Ashley P. Gumsley ¹, David Chew ³, Petko Petrov ⁴, Aleksandra Gawęda ¹, Anna Zagórska ², Ewa Deput ², Nikolay Gospodinov ⁵ and Kamila Banasik ¹

¹ Institute of Earth Sciences, Faculty of Natural Sciences, University of Silesia in Katowice, Będzińska 60, 41-200 Sosnowiec, Poland; ashley.gumsley@us.edu.pl (A.P.G.); aleksandra.gaweda@us.edu.pl (A.G.); kamila.banasik@us.edu.pl (K.B.)

² Institute of Geological Sciences PAS, 00-818 Warsaw, Poland; anna.salacinska@twarda.pan.pl (A.S.); a.zagorska@ingpan.krakow.pl (A.Z.); depute@twarda.pan.pl (E.D.)

³ Department of Geology, School of Natural Sciences, Trinity College Dublin, 2 Dublin, Ireland; chewd@tcd.ie

⁴ The Earth and Man National Museum in Sofia, 1421 Sofia, Bulgaria; petkopet@abv.bg

⁵ Hristo Smirnenski 37-41, G, 51 Topolovgrad, Bulgaria; cho2@mail.bg

* Correspondence: krzysztof.szopa@us.edu.pl; Tel.: +48-603-813-074

Received: 24 December 2019; Accepted: 4 March 2020; Published: 15 March 2020



Abstract: Southeastern Bulgaria is composed of a variety of rocks from pre-Variscan (ca. 0.3 Ga) to pre-Alpine *sensu lato* (ca. 0.15 Ga) time. The Sakar Unit in this region comprises a series of granitoids and gneisses formed or metamorphosed during these events. It is cut by a series of post-Variscan hydrothermal veins, yet lacks pervasive Alpine deformation. It thus represents a key unit for detecting potential tectonism associated with the enigmatic Cimmerian Orogenic episode, but limited geochronology has been undertaken on this unit. Here we report age constraints on hydrothermal activity in the Sakar Pluton. The investigated veins contain mainly albite–actinolite–chlorite–apatite–titanite–quartz–tourmaline–epidote and accessory minerals. The most common accessory minerals are rutile and molybdenite. Apatite and titanite from the same vein were dated by U–Pb LA–ICP–MS geochronology. These dates are interpreted as crystallization ages and are 149 ± 7 Ma on apatite and 114 ± 1 Ma on titanite, respectively. These crystallization ages are the first to document two stages of hydrothermal activity during the late Jurassic to early Cretaceous, using U–Pb geochronology, and its association with the Cimmerian orogenesis. The Cimmerian tectono-thermal episode is well-documented further to the east in the Eastern Strandja Massif granitoids. However, these are the first documented ages from the western parts of the Strandja Massif, in the Sakar Unit. These ages also temporally overlap with previously published Ar–Ar and K–Ar cooling ages, and firmly establish that the Cimmerian orogeny in the studied area included both tectonic and hydrothermal activity. Such hydrothermal activity likely accounted for the intense albitization found in the Sakar Unit.

Keywords: geochronology; U–Pb dating; Cimmerian; apatite; titanite; Sakar; Bulgaria

1. Introduction

The Balkan Peninsula consists of a series of variably metamorphosed terranes that predominantly formed in the Phanerozoic due to the collision of Gondwana against Baltica, then Laurussia, and later proto-Africa against proto-Europe during the Caledonian, Variscan, and Alpine orogeny [1]. Southern Bulgaria is divided into the Rhodope and Strandja massifs, with the relationship between them remaining uncertain [2]. These massifs are composed of highly deformed orthogneisses and paragneisses. The highly metamorphosed and deformed pre-Variscan basement is intruded by

Variscan granites, which formed as a result of the collision of Gondwana and Laurussia during Pangea assembly [3]. Later, Cimmerian-aged events preceded the main collision of Africa and Europe during the Alpine Orogeny [4]. The Cimmerian Orogeny (~200–150 Ma; [5] and references therein) occurred to the south and east of Bulgaria, with most Cimmerian tectonism documented between Turkey and Central Asia [4–7]. The enigmatic Cimmerian Orogeny in Southeastern Europe, however, is difficult to identify mostly due to the pervasive later Alpine orogenic overprint [8]. In Southeastern Bulgaria, the late Variscan Sakar pluton intrudes the pre-Variscan basement [9] and is in turn affected by later events of deformation and metamorphism, which in the past have been attributed to the Alpine Orogeny [10]. Many of the Sakar granitoids are affected by a series of veins and pervasive albitization, connected with Na-metasomatism of undetermined age [11,12]. Herein, we provide the first U–Pb LA-ICP-MS dates from apatite and titanite in one vein type, documenting two episodes of hydrothermal activity within the Sakar Unit of the Strandja Massif, which critically escaped significant Alpine overprinting.

2. Geological Setting

The Sakar Unit of the Strandja Zone [13], also known as the Strandja (Strandzha) Massif (SM; [14,15] and references therein) or Istranca Massif (IM; [16]), is located in the southeastern part of Bulgaria, close to the border with Turkey and Greece (Figure 1A). It belongs to the East Srednogorie Zone of the Balkan Orogenic System [17,18]. The Sakar Unit is exposed in the Sakar Mountains, which neighbor the Rhodope and Strandja Mountains, and is bounded by the Maritsa and Tundzha rivers (Figure 1A). The Sakar Unit consists of the Sakar Pluton, which intruded into high-grade meta-igneous and metasedimentary rocks, and in turn are unconformably overlain by Triassic to middle Jurassic metasedimentary rocks (Figure 1B). The Sakar Pluton is an East–West elongated magmatic body, ca. 20 km long and up to ca. 15 km wide, forming the major component of the Sakar Unit. In the west and north of the unit, the contact between the pluton and the host rocks is covered by Neogene sedimentary rocks (Figure 1), whereas in the northeast and south, the intensely sheared contacts of the pluton are exposed [13,19,20]. The Sakar Pluton consists of various granitoids divided into three groups: equigranular granitoids, porphyritic granitoids also with feldspar megacrysts, and aplitic leucogranites. The Sakar granitoids contain xenoliths of the country rock and are cut by numerous aplite veins and some mafic dykes [11]. Locally, the granitoids are affected by extensive albitization (e.g., documented from the northeastern part of pluton, south of the Orlov dol village and Kanarata quarry near Hlyabovo [11,12]). The timing of albitization is unknown; however, this process also affected the low-grade Triassic metasedimentary rocks, and is therefore post-Triassic [11,12].

The crystallization age of the Sakar Pluton, as well as the age of the meta-igneous and metasedimentary rocks has been the subject of long debate. Isotope dating by the Rb–Sr method from the Sakar Pluton has yielded contradictory results of 320 ± 18 Ma [21], 499 ± 70 Ma [21], and 250 ± 35 Ma [22], which is discussed by Ivanov et al. [23], who proposed a post-middle-Triassic emplacement age for the Sakar Pluton. K–Ar ages range between ca. 144 Ma and ca. 111 Ma [21,24–27] and likely reflect a regional thermal overprint. However, preliminary U–Pb zircon dating results presented by Peytcheva et al. [28], Bonev et al. [9], and Pristavova et al. [20] yield late-Carboniferous to early Permian (ca. 305 Ma to ca. 295 Ma) crystallization ages for the Sakar Pluton. These new results contradict the timing of supposed Jurassic to early Cretaceous emplacement of the granitoid presented by Ivanov [23] which was supported by field observations of Gerdjikov [13]. These new late-Variscan (ca. 300 Ma) ages also provide a minimum age for the host rocks of the Sakar Pluton (the Strandja Massif). The Strandja Massif has widely been accepted as Precambrian in age [29], although there are no modern geochronological studies, apart from the recent study by Bonev et al., [9], which indicates the presence of an Ordovician magmatic event in the massif. Thus the Paleozoic, pre-Carboniferous evolution of the Strandja Massif thus remains uncertain.

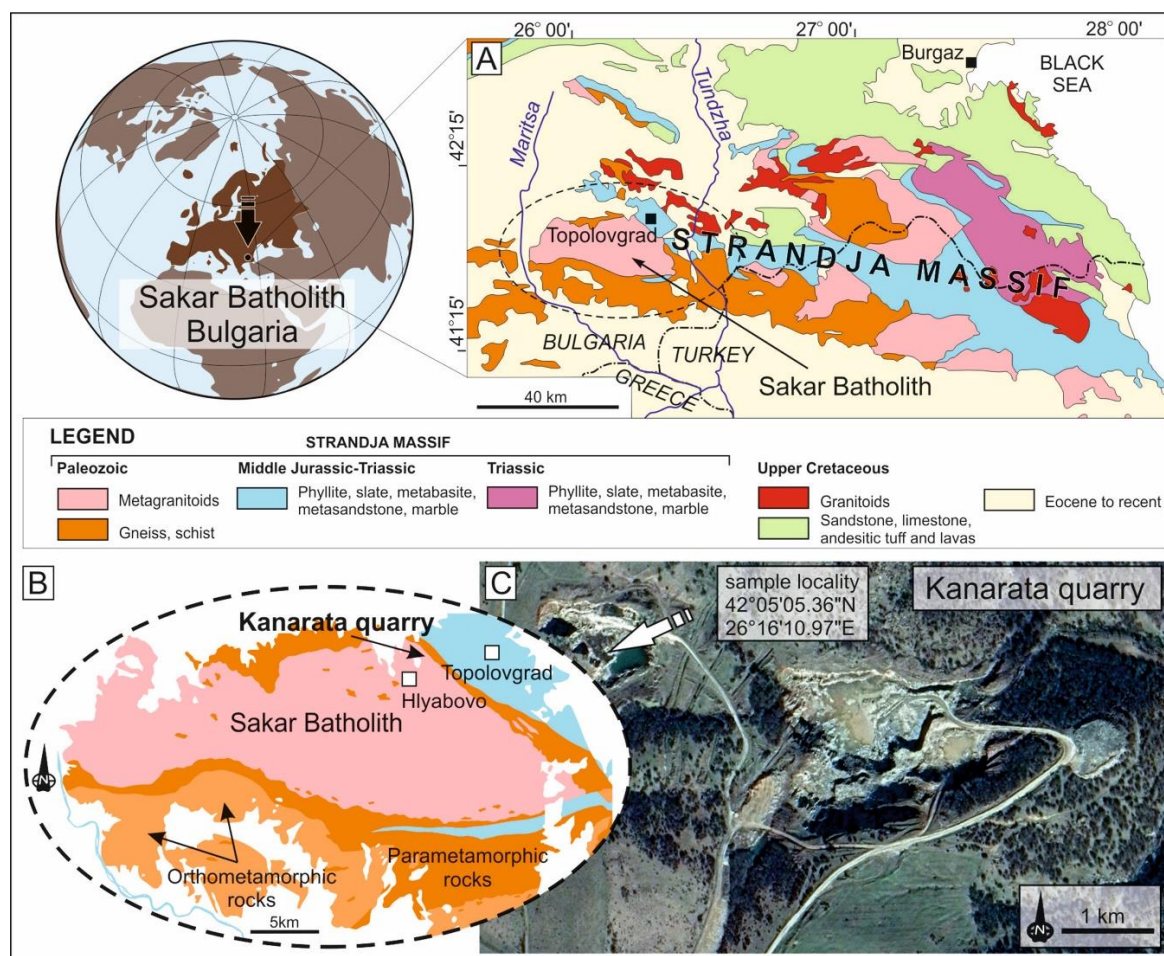


Figure 1. The Sakar Mountains in Bulgaria—study area: (A) geological map of the Strandja Massif (Southeast Bulgaria) and neighboring regions; (B) geological sketch map of the Sakar Unit (modified after [10,11]); (C) Kanarata quarry—sample locality.

3. Sample Locality and Methods

Rock samples for this study were collected from the Kanarata quarry (Figure 1C), located ca. 3 km north of Hlyabovo village and ca. 5 km east of Topolovgrad (Haskovo District), within the northeastern part of the Sakar Pluton. The quarry is located near the contact with the country rock (<500 m to the west of the quarry), and contains granitoids with abundant amphibolite xenoliths, which are a common feature of the margin of the pluton. The quarry is currently active, with the granites being exploited as dimension stone. The locality is also known for the occurrence of gemstone-quality apatite ([30]; Figure 2A).

Pale-blue apatite and olive-green titanite crystals (Figure 2B) from the Hlyabovo (Alpine-type) fissures were collected for U–Pb laser ablation–inductively coupled plasma mass spectrometry (LA-ICP-MS) dating.

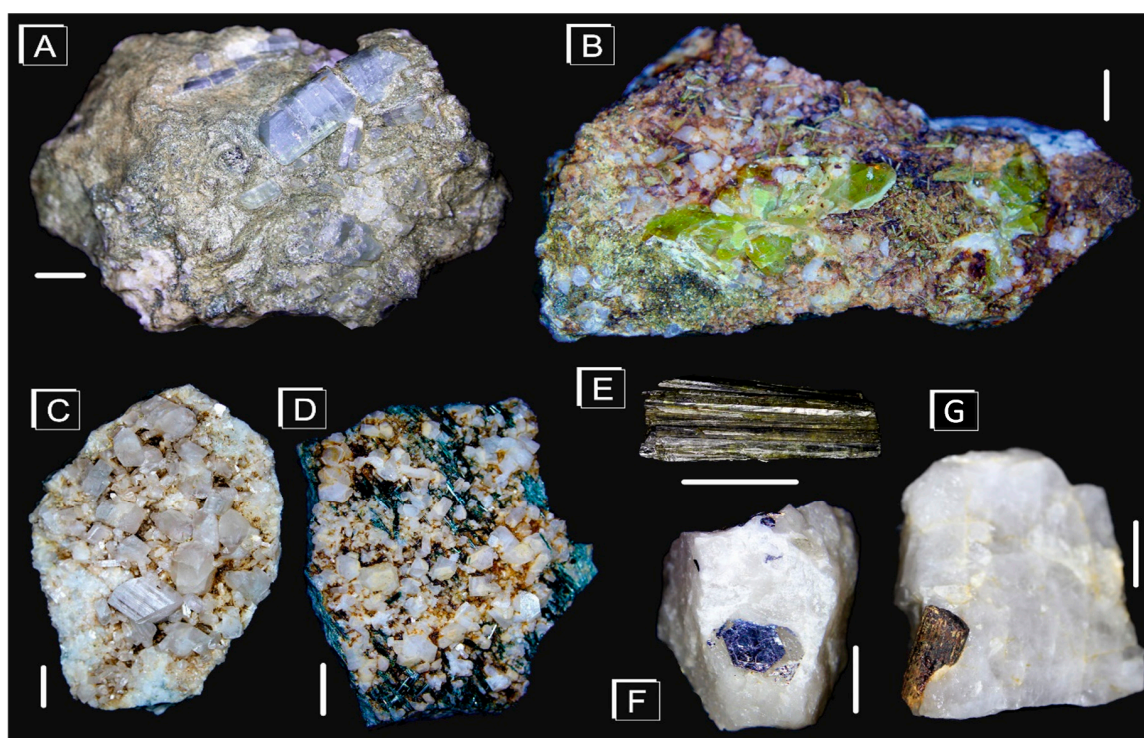


Figure 2. Example of minerals within the investigated veins. (A) Blue apatite crystal on albite and chlorite, (B) green titanite, (C) albite crystals, (D) actinolite overgrown by albite, (E) epidote aggregate, (F) molybdenite flake on milky quartz, and (G) rutile crystals in quartz. Scale bars are 1 cm.

3.1. Microscopy

Petrographic analyses of thin sections, using light microscopy, were undertaken at the Faculty of Natural Sciences in the University of Silesia in Katowice, Sosnowiec, Poland, using an Olympus BX–51 microscope to constrain mineralogical, textural, and microstructural relationships of the samples and to determine the presence of dateable accessory minerals. The petrographic observations were used to select representative minerals for subsequent electron probe microanalysis (EMPA) and whole-rock major and trace-element geochemical analyses.

3.2. Electron Probe Micro-Analyses (EMPA)

Microprobe analyses of the main rock-forming and accessory minerals were carried out at the Inter-Institutional Laboratory of Microanalyses of Minerals and Synthetic Substances, University of Warsaw, Warsaw, using a CAMECA SX–100 electron microprobe. The analytical conditions employed an accelerating voltage of 15 kV, a beam current of 20 nA, counting times of 4 s for peak and background, and a beam diameter of 1–5 μm . The full analytical procedures are listed in Table S1.

3.3. LA-ICP-MS U–Pb Apatite and Titanite Dating

U–Pb apatite and titanite ages were determined by using a Photon Machines Analyte Exite 193 nm ArF Excimer laser-ablation system with a Helix 2-volume ablation cell coupled to an Agilent 7900 ICP-MS, using an Aerosol Rapid Introduction System (ARIS; Teledyne Photon Machines), at the Department of Geology, Trinity College, Dublin, Ireland. The ICP-MS was tuned, using NIST 612 standard glass to yield Th/U ratios of unity and low oxide production rates (ThO^+/Th^+ typically $<0.15\%$). A 0.15 L/min He carrier gas was fed into the cell body, and 0.25 L/min He was fed into the cup, the aerosol was subsequently mixed with 0.6 L/min Ar make-up gas and a small volume of N_2 (~ 7 mL/min) in a ~ 1 cm^3 signal-smoothing device coupled to the ARIS, to enhance signal sensitivity and reduce oxide formation. For apatite, the following 30 isotopes were measured (with their respective

dwell times in milliseconds listed in parentheses): ^{31}P (10), ^{35}Cl (20), ^{43}Ca (10), ^{51}V (7.5), ^{55}Mn (75), ^{88}Sr (7.5), ^{89}Y (5), ^{90}Zr (10), ^{137}Ba (10), ^{139}La (5), ^{140}Ce (5), ^{141}Pr (5), ^{146}Nd (5), ^{147}Sm (7.5), ^{153}Eu (10), ^{157}Gd (10), ^{159}Tb (10), ^{163}Dy (10), ^{165}Ho (10), ^{166}Er (10), ^{169}Tm (10), ^{172}Yb (10), ^{175}Lu (15), ^{202}Hg (5), ^{204}Pb (5), ^{206}Pb (75), ^{207}Pb (75), ^{208}Pb (5), ^{232}Th (5), and ^{238}U (75), corresponding to a total dwell time of 456 ms and a total cycle time of 510 ms. For titanite, the following 25 isotopes were measured (with their respective dwell times in milliseconds listed in parentheses): ^{43}Ca (10), ^{49}Ti (10), ^{90}Zr (5), ^{139}La (5), ^{140}Ce (5), ^{141}Pr (5), ^{146}Nd (5), ^{147}Sm (5), ^{153}Eu (5), ^{157}Gd (5), ^{159}Tb (5), ^{163}Dy (5), ^{165}Ho (7), ^{166}Er (7), ^{169}Tm (7), ^{172}Yb (7), ^{175}Lu (10), ^{202}Hg (25), ^{204}Pb (25), ^{206}Pb (50), ^{207}Pb (70), ^{208}Pb (20), ^{232}Th (10), and ^{238}U (30), corresponding to a total dwell time of 343 ms and a total cycle time of 379.5 ms. For both titanite and apatite analyses, the laser fluence was 2.5 J/cm², with a repetition rate of 15 Hz, a 47 μm spot size, and an analysis time of 20 s, followed by an 8 s background measurement.

The raw isotope data were reduced, using the “VizualAge UcomPbine” data-reduction scheme (DRS) of Chew et al. [31], a modification of the U–Pb geochronology “VizualAge” DRS of Petrus and Kamber [32] that can account for the presence of variable common Pb in the primary standard materials. The DRS runs within the freeware IOLITE package of Paton et al. [33]. In IOLITE, user-defined time intervals are established for the baseline correction procedure to calculate session-wide baseline-corrected values for each isotope. The time-resolved fractionation response of individual standard analyses is then characterized, using a user-specified down-hole correction model (such as an exponential curve, a linear fit, or a smoothed cubic spline). The VizualAge data-reduction scheme then fits this appropriate session-wide “model” U–Th–Pb fractionation curve to the time-resolved standard data and the unknowns. Sample-standard bracketing is applied after the correction of down-hole fractionation to account for long-term drift in isotopic or elemental ratios by normalizing all ratios to those of the U–Pb reference materials. Common Pb in the apatite and titanite standards was corrected by using the ^{207}Pb -based correction method.

Blocks of nine standards and two NIST612 standard glass analyses were followed by 20 unknown samples. For apatite analyses, the Madagascar natural mineral standard [34] was used (weighted mean ID-TIMS concordia age of this crystal is 473.5 ± 0.7 Ma). McClure Mountain syenite apatite (weighted mean $^{207}\text{Pb}/^{235}\text{U}$ age of 523.51 ± 2.09 Ma [35], and Durango apatite (31.44 ± 0.18 Ma [36], were used as secondary standards. As the in-house standards, McClure Mountain apatite yielded a U–Pb Tera–Wasserburg concordia lower intercept age of 523.5 ± 3.0 Ma (MSWD = 2.4), anchored using a $^{207}\text{Pb}/^{206}\text{Pb}$ value of 0.88198 derived from an apatite ID-TIMS total U–Pb isochron [35]. The Durango apatite standard yielded a U–Pb Tera–Wasserburg concordia lower intercept age of 33.43 ± 0.62 Ma (MSWD = 1.8), anchored using a $^{207}\text{Pb}/^{206}\text{Pb}$ value of value of 0.838 derived from the Stacey and Kramers [37] terrestrial Pb evolution model at an age of 31.44 Ma. For titanite analyses, MKED1 titanite ($^{207}\text{Pb}/^{206}\text{Pb}$ TIMS age of 1521.02 ± 0.55 Ma; [38]) was used as the primary standard. OLT–1 titanite (U–Pb TIMS concordia age of 1014.8 ± 2.0 Ma; [39]) and BLR titanite (U–Pb TIMS age of 1047.1 ± 0.4 Ma; [40]) were used as the secondary U–Pb calibration standards and yielded weighted average ^{207}Pb -corrected ages of 1017.4 ± 6.7 Ma ($n = 17$, MSWD = 3.4) and 1067.9 ± 6.2 Ma ($n = 14$, MSWD = 2.4), respectively.

4. Results

4.1. Petrography

The studied rocks are hosted by the so-called Aleksandrovo-type granites (see [12] and references therein), which in Kanarata quarry are represented by medium-grained albitized granitoids (Figure 3A). These rocks contain amphibolite xenoliths from tens of centimeters up to 3 m in length (Figure 3B). All of the xenoliths have sharp contacts with the country rock and exhibit a distinctive mineral lineation (Figure 3B,C).

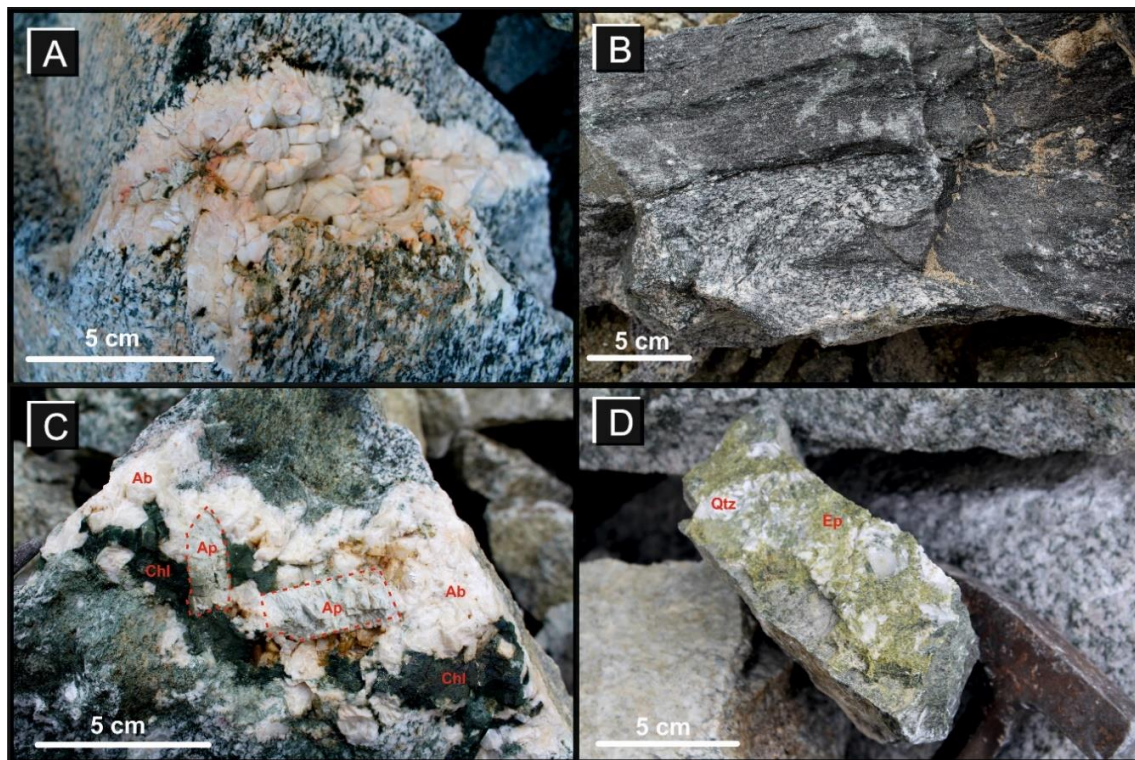


Figure 3. Photographs of the most common rock types in the investigated Kanarata quarry. (A) monzonite with an albite nest, (B) amphibolite xenolith within the contact zone, (C) an example of Alpine-type fissures, and (D) the second vein type with massive quartz and epidote. Ap = apatite, Chl = chlorite, Ab = albite, Ep = epidote, and Qtz = quartz.

All investigated veins are Alpine-type fissures, varying from a few centimeters to up to 1 m in length (Figure 3A,C). These veins are rich in albite, actinolite, chlorite, apatite, and titanite. The albite is composed of milky to translucent crystals, with an anorthite content up to 3.5 wt.% (Table S2). The albite crystals are euhedral, and up to 1 cm in length (Figure 2D,E). Actinolite (Mg-rich hornblende; Table S3), forms different varieties of pale- to dark-green crystals. They typically have a needle-like habit, with long prismatic crystals up to 2–3 cm in length and an aspect ratio as high as 100:1. The actinolite commonly occurs as inclusions in albite. The chlorite in the vein contains 50%–82% of the clinochlore ($\text{Mg}_5\text{Al}(\text{Si}_3\text{Al})\text{O}_{10}(\text{OH})$) end-member, 12%–49% of the chamosite ($\text{Fe}^{2+}_5\text{Al}(\text{Si}_3\text{Al})\text{O}_{10}(\text{OH})$) end-member, and <3% of the pennantite ($\text{Mn}_5\text{Al}(\text{Si}_3\text{Al})\text{O}_{10}(\text{OH})$) end-member (classification after Bailey [41]; Table S4). The chlorite flakes partially overgrow albite and actinolite, and mostly form aggregates up to 300 μm in length. Chlorite thermometry, using the Cathelineau and Nieva's [42], Jowett's [43], and Karaniditis et al.'s [44] methodologies, yielded temperature ranges of 298–340 $^\circ\text{C}$, 286–329 $^\circ\text{C}$, and 272–300 $^\circ\text{C}$, respectively (Table S4; Figure 5). Apatite generally forms well-shaped hexagonal milky to bluish crystals, which commonly are prismatic, dipyrarnidal, and stubby. Sporadically, flat or tabular plates were also noted (Figure 2A). The apatite crystals are up to 5–7 cm in length, with an aspect ratio of 4:1. Twinned crystals are lacking. All investigated crystals are fluorapatite (Ca-apatite; Table 1), and imaging by EMPA reveals the chemical homogeneity of the investigated apatite crystals. Titanite from the same locality usually forms euhedral crystals, twinned on {221}. Some of the crystals may be in flattened into tabular or even prismatic forms, with pointed terminations and complex dipyrarnidal crystals. The titanite crystals are pale to dark green, and are up to 2 cm in length (Figure 2B). The crystals do not reveal any chemical zonation (Table S2). The titanite in most cases is not overgrown by any associated minerals. Titanite crystals contain more chlorite inclusions than the apatite, regardless of the crystal size. Moreover, both phases do not form intergrowths between each other. The presence of rutile is limited to prismatic metallic

crystals, with lengths up to 200 μm . The rutile crystals are often strongly weathered. This type of vein (the Alpine-type fissures) is often located close to amphibolite xenoliths.

Sporadically, veins composed mainly of quartz, epidote–clinozoisite, tourmaline (schörl), albite, rutile, and molybdenite are also noted, although these were not dated in this study. The groundmass of these veins is mainly quartz. Barren quartz sporadically forms euhedral crystals (up to 4–5 cm in length) that are smoky to in color transparent. The more common massive quartz is mostly gray–milky in color (Figure 2F,G). Quartz is associated only with this type of vein. Albite forms white crystals, which are orientated perpendicular to the contact with the host rock. A similar situation is observed if rutile crystals are present, with the rutile crystals reaching up to 4 cm in length (Figure 2E). Prismatic, elongated crystals of rutile, with a prominent trigonal prism and pyramid, were observed. The surface of the rutile crystals appears to be oxidized and coated by a thin film of Fe-hydroxides (goethite/limonite?). Epidote group minerals are present in this vein-type as radial aggregates of acicular to columnar crystals, having pale-green to green color (Figure 2E). Molybdenite in this vein type is up to 2.5 cm across, and the crystals are commonly tabular- and barrel-shaped (Figure 2F). Tourmaline group minerals are represented by schörl, which forms prismatic to acicular crystals, and sporadically may be modified along the [0001] plane, with a prominent trigonal prism and pyramid. The crystals are up to 8 cm in length, with an aspect ratio of 10:1. Tourmaline mostly occurs only with quartz.

4.2. U–Pb Geochronology

The homogeneity and size of the titanite (Table 1) and apatite (Table 2) grains in this study make them useful for U–Pb dating. Sixty titanite grains were analyzed, and all the data points are highly discordant due to high proportions of common Pb relative to radiogenic Pb. All data lie on an unanchored Tera–Wasserburg discordia line with a lower intercept age of 114 ± 1 Ma (MSWD = 1.3) and a $^{207}\text{Pb}/^{206}\text{Pb}$ initial ratio of 0.6799 ± 0.011 (Figure 4A).

Apatite grains were also analyzed, and the 49 data points were also highly discordant due to the high proportion of common Pb compared to radiogenic Pb. The data points all fall on an unanchored Tera–Wasserburg discordia, with a lower intercept age of 149 ± 7 Ma (MSWD = 1.7) and a $^{207}\text{Pb}/^{206}\text{Pb}$ initial ratio of 0.772 ± 0.021 (Figure 4B). All LA–ICP–MS data are listed in Table S5.

Table 1. Representative electron microprobe analyses (EMPA) of apatite and number of a.p.f.u. are calculated on the basis of 25O^{2-} of the investigated sample from the Kanarata quarry, Bulgaria.

Compound	1	2	3	4	5	6	7	8	9	10
CaO (wt.%)	55.69	55.82	55.57	55.57	55.83	55.77	55.75	56.13	56.11	56.26
SiO ₂	0.23	0.10	b.d.l.							
P ₂ O ₅	41.51	42.32	41.83	42.56	42.58	42.31	41.87	42.61	42.42	42.07
SO ₃	0.12	0.13	b.d.l.							
F	2.83	2.82	3.05	2.55	2.27	2.88	1.99	2.79	2.64	2.40
H ₂ O	0.39	0.41	0.27	0.54	0.68	0.37	0.80	0.43	0.50	0.61
O=F,Cl	1.19	1.19	1.29	1.07	0.96	1.22	0.84	1.18	1.11	1.01
Total	99.58	100.42	99.44	100.14	100.41	100.11	99.57	100.79	100.56	100.33
Ca (a.p.f.u.)	10.37	10.27	10.36	10.20	10.21	10.31	10.26	10.29	10.30	10.34
Si	0.04	0.02	-	-	-	-	-	-	-	-
P	6.11	6.15	6.16	6.18	6.15	6.18	6.09	6.17	6.15	6.11
S	0.02	0.02	-	-	-	-	-	-	-	-
X _F	1.55	1.53	1.68	1.38	1.22	1.57	1.08	1.51	1.43	1.30
X _{OH}	0.45	0.47	0.32	0.62	0.78	0.43	0.92	0.49	0.57	0.70

Note: b.d.l.—below detection limit.

5. Discussion

5.1. Age Significance: Apatite vs. Titanite

Titanite (CaTiSiO_5) and apatite ($\text{Ca}_5(\text{PO}_4)_3(\text{Cl/F/OH})$) are common accessory minerals in a compositionally wide range of igneous, metamorphic (especially in amphibolite facies), and hydrothermal rocks. Both minerals are also important carriers for numerous trace elements, including U, Th, and Pb. Titanite commonly contains trace amounts of U and largely excludes initial Pb, thus making it useful for radiometric dating using the U–Pb–Th isotopic system (e.g., [45–47]). Multi-equilibrium thermobarometry suggests that the titanite closure temperature falls within a restricted range of 660–700 °C (e.g., [48]). For apatite, experimental determination of the diffusion parameters of Pb by high-temperature annealing experiments [49] and ion implantation with Rutherford backscattering techniques [50] imply closure temperatures of between 450 and 550 °C. Apatite is chemically stable at middle-amphibolite facies conditions (i.e., temperatures above its closure temperature). Under such conditions, it is thought the U–Pb systematics of apatite are controlled predominantly by volume diffusion rather than by the new growth or recrystallization [51]. Taking the above factors into consideration, the titanite and apatite ages represent separate crystallization episodes in the same vein type, as the calculated ages lie significantly outside of their mutual analytical uncertainties. In addition, the significantly lower $^{207}\text{Pb}/^{206}\text{Pb}$ initial ratio of the titanite (suggesting derivation from a radiogenic fluid), also implies separate crystallization episodes.

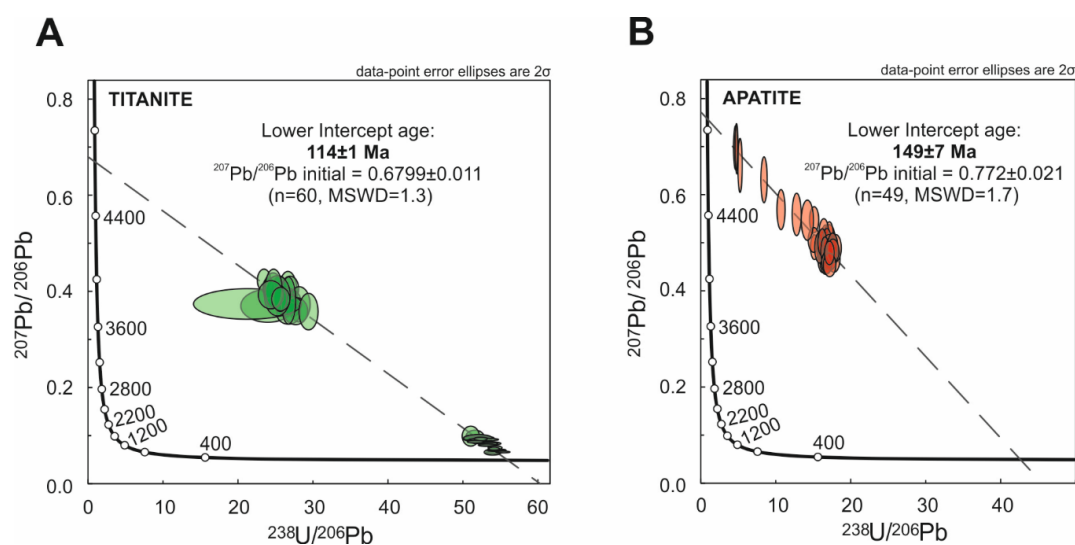


Figure 4. Tera–Wasserburg concordia plots for LA–ICP–MS U–Pb titanite (A) and apatite (B) analyses from the Kanarata quarry. Data-point error ellipses are 2σ .

The Alpine-type fissure veins contain abundant apatite, titanite, albite, actinolite, and chlorite, and they exhibit similarities with vein systems across most orogenic zones connected with the Alpine collision in most of Southern Europe, from Italy to Greece, to Turkey, and onward to Iran and China (e.g., [52–56]). This veining is associated with hydrothermal activity, which is interpreted in this study as being the cause of Na-albitization in the country rocks. The occurrence of two mineral phases of different ages in one druse indicates two discrete hydrothermal crystallization episodes. Chlorite temperature calculations show that the most probable temperature for hydrothermal activity occurred in the range of ca. 290–330 °C (Figure 5).

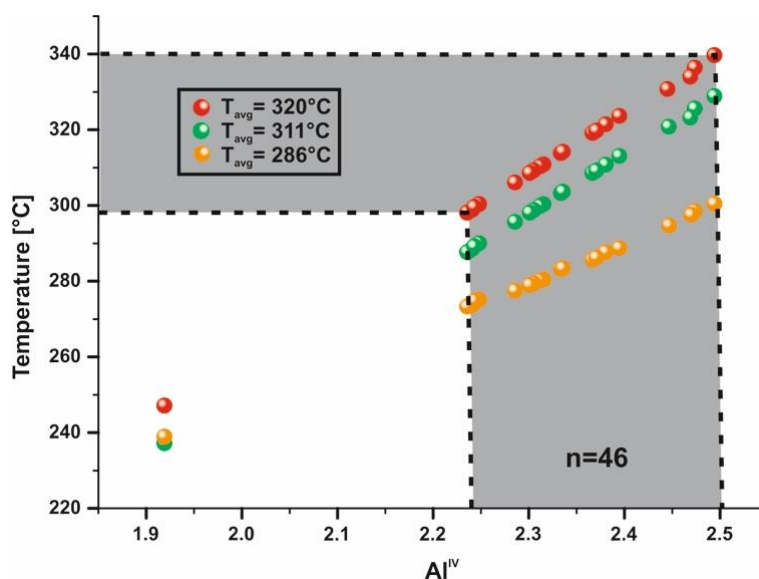


Figure 5. Al^{IV} vs. temperature plot for the chlorites investigated in this study. Temperatures is based on three geothermometers: [42] (red), [43] (green), and [44] (orange).

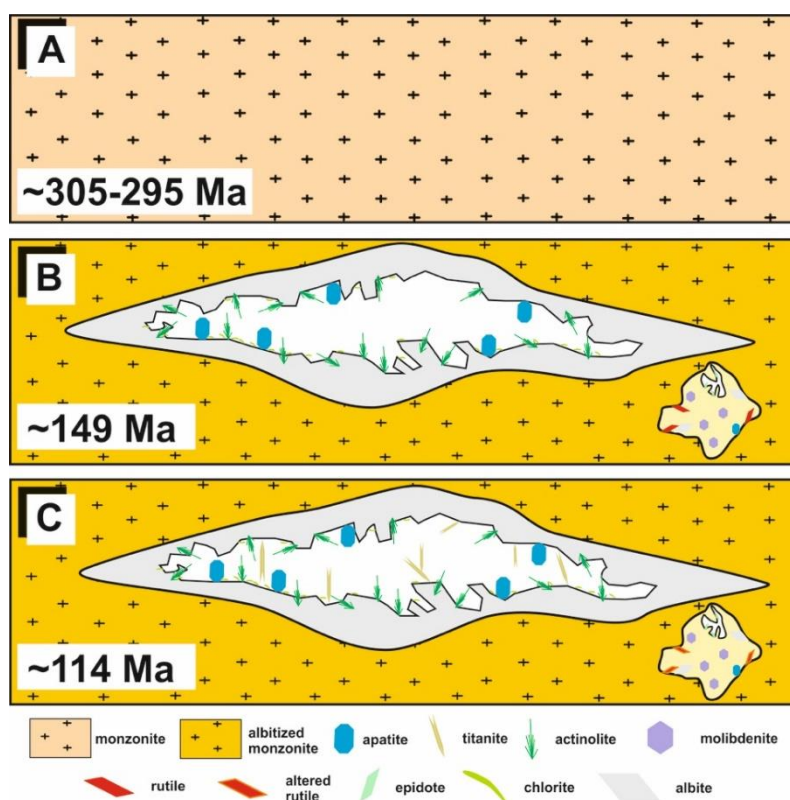
5.2. Geotectonic Implications of the Apatite and Titanite Ages

The margins of the late-Carboniferous to early Permian Sakar Pluton (305–295 Ma [9,12,28]; Figure 6A) are affected by extensive Na-albitization, as documented by Kamenov et al., [11] and Pristvova et al., [12], along with the vein systems such as those are observed at Kanarata quarry (Figure 6B,C). The obtained U–Pb LA-ICP-MS ages of 149 ± 7 Ma on apatite and 114 ± 1 Ma on titanite, respectively, suggest two discrete crystallization ages within the Sakar Pluton. The hydrothermal veins, therefore, represent either a long-lived (i.e., ca. 35 Myr) hydrothermal episode within the Sakar Unit in the late-Jurassic to early Cretaceous, or two different episodes of fracturing associated with hydrothermal activity. Albitization from Kanarata quarry was documented by Pristavova et al., [12]; however, the timing of this alteration process remained unknown. As field relationships suggest the spatial and temporal link of albitization and veining here, we suggest the hydrothermal activity within the Sakar Unit is coeval with K–Ar ages between ca. 144 and ca. 111 Ma [21,22,24–27]. Similar late-Jurassic to early Cretaceous ages are also documented from the eastern part of the Strandja Zone, where a two-stage process of ductile and brittle deformation is documented by Elmas et al., [57], between ca. 156 and ca. 143 Ma and between ca. 136 and ca. 119 Ma, respectively. This deformation was interpreted by Elmas et al., [57] as being coincident with core complex formation during extension. However, this contradicts previous interpretations by Dabovski et al., [18] and Okay et al., [14], who connected ca. 155 Ma Rb–Sr ages as being related to regional metamorphism and thrusting during orogenesis.

Table 2. Representative electron microprobe analyses (EMPA) of titanite and number of ion a.p.f.u. calculated on the basis of 18 O²⁻ of the investigated sample from the Kanarata quarry, Bulgaria.

Compound	1	2	3	4	5	6	7	8	9	10
SiO ₂ (wt.%)	30.20	30.19	29.93	30.18	30.04	30.12	30.31	30.19	30.23	29.91
TiO ₂	38.65	38.47	38.47	36.88	38.38	38.81	38.21	38.54	38.54	38.59
CaO	28.33	28.26	28.07	28.24	28.25	28.41	28.24	28.24	28.26	28.21
Al ₂ O ₃	1.11	1.23	1.02	1.75	0.95	0.87	1.18	1.03	0.84	0.86
MnO	b.d.l.	b.d.l.	b.d.l.	b.d.l.	b.d.l.	b.d.l.	0.12	0.12	b.d.l.	b.d.l.
Fe ₂ O ₃	0.68	0.60	0.76	0.64	0.61	0.74	0.71	0.34	0.76	0.43
Y ₂ O ₃	0.13	0.16	0.11	0.16	0.17	b.d.l.	0.14	0.15		0.14
V ₂ O ₅	0.19	0.25	0.27	0.26	0.30	0.24	0.29	0.19	0.31	0.24
F	0.24	0.18	0.10	0.41	0.12	0.02	0.22	0.16	0.26	0.10
O=F	0.10	0.08	0.04	0.17	0.05	0.01	0.09	0.07	0.11	0.04
Total	99.42	99.25	98.69	98.35	98.78	99.21	99.32	98.88	99.09	98.44
Si (a.p.f.u.)	3.58	3.58	3.57	3.62	3.58	3.57	3.60	3.60	3.60	3.58
Ti	3.45	3.43	3.45	3.33	3.44	3.46	3.41	3.45	3.45	3.47
Ca	3.60	3.59	3.58	3.63	3.61	3.61	3.59	3.60	3.60	3.61
Al	0.16	0.17	0.14	0.25	0.13	0.12	0.17	0.14	0.12	0.12
Mn	-	-	-	-	-	-	0.01	0.01	-	-
Fe	0.06	0.05	0.07	0.06	0.06	0.07	0.06	0.03	0.07	0.04
Y	0.01	0.01	0.01	0.01	0.01	0.01	0.01	0.01		0.01
V	0.02	0.02	0.02	0.02	0.02	0.02	0.02	0.02	0.02	0.02
F	0.09	0.07	0.04	0.16	0.04	0.01	0.08	0.06	0.10	0.04
Total	10.96	10.92	10.87	11.08	10.90	10.85	10.96	10.92	10.95	10.88

Note: b.d.l.—below detection limit.

**Figure 6.** Simplified model of the hydrothermal activity in the Sakar Unit of Southeastern Bulgaria, based on the geochronological data presented in this study and field observations. (A) Formation of the Variscan host rock (~305–295 Ma). (B) The first, older hydrothermal event forms the primary mineralization (ca. 149 Ma). (C) The second, younger hydrothermal episode forms titanite (ca. 114 Ma age).

The ages presented here are coeval with other regional events, such as those documented further west in the Rhodope Massif [58,59], to the north in the Carpathians [60–62], and to the east in Turkey and Iran [63], and they are likely connected to the Cimmerian Orogeny [4]. The Cimmerian Orogeny is mostly documented from Central Asia, where oceanic island arcs were subducted beneath Asia prior to the arrival of India and the of the Neo-Tethys basin [4]. However, recent work shows that the orogen extended much further to the west, including into Iran, Turkey and into Bulgaria [8]. In Şengör [4,64], the Cimmerian Orogeny was defined by the continent–continent collision of a Gondwana-derived continental ribbon on to Laurasia. However, more recent work indicates a series of Cimmerian tectonic events [62,65–69]. The Cimmerian Orogeny is succeeded by the Alpine Orogeny, which stretches further to the west, and includes the Pyrenees, Alps, Carpathians, Balkanides, Pontides, Zagros, and ultimately, the Himalayas, as the bulk of Africa and India collided with Europe and Asia, respectively. However, distinguishing between Cimmerian- and Alpine-related structures is difficult. The Sakar Unit, along with the majority of the Strandja Massif further to the east, appears to have escaped any significant Alpine orogenesis, *sensu stricto* [8]. Although the final stages of the Cimmerian Orogeny likely overlapped in age with the Alpine Orogeny *sensu lato*, the ages from this study predate the Alpine Orogeny and are not affected by it. The Alpine Orogeny is documented further to the north in the Carpathians and Srednogorie mountains [70,71] and to the west, in the Rhodope Massif [72].

6. Conclusions

1. The U–Pb ages in this study are interpreted as distinct crystallization episodes, at 149 ± 7 Ma on apatite and 114 ± 1 Ma on titanite, respectively. They are the first evidence for two stages of hydrothermal activity during the late-Jurassic to early Cretaceous in Southeastern Bulgaria and are broadly coeval with the Cimmerian orogenesis. The ages obtained in this study are broadly coeval with other units from the eastern part of the Strandja Massif, where two stages of deformation are documented.

2. The U–Pb apatite concordia systematics are robust, with both the U–Pb apatite and U–Pb titanite data implying they were unaffected by open system processes above their respective closure temperatures.

3. The study also confirms the lack of any significant Alpine orogenic footprint on the western part of the Strandja Massif, making it distinct from the neighboring Rhodope and Balkanides mountains.

Supplementary Materials: The following are available online at <http://www.mdpi.com/2075-163X/10/3/266/s1>. Table S1: EMPA patterns, crystals, and reference materials. Table S2: Representative electron microprobe analyses (EMPA) of albite and the number of a.p.f.u. calculated on the basis of 8 O^{2-} of the investigated sample from the Kanarata quarry, Bulgaria. Table S3: Representative electron microprobe analyses (EMPA) of actinolite and the number of a.p.f.u. calculated on the basis of 12 O^{2-} of the investigated sample from the Kanarata quarry, Bulgaria. Table S4: Representative electron microprobe analyses (EMPA) of chlorites and number of a.p.f.u. calculated on the basis of 12 O^{2-} of the investigated sample from the Kanarata quarry, Bulgaria. Table S5: Representative LA-ICP-MS U–Pb apatite and titanite data from the Kanarata quarry, Bulgaria.

Author Contributions: Conceptualization, K.S., A.S., and A.P.G.; methodology, K.S., D.C., A.P.G., A.Z., and E.D.; formal analysis, K.S., D.C., and K.B.; investigation, all authors.; writing—original draft preparation, K.S., A.P.G., N.G. and A.S.; writing—review and editing, K.S., A.S., P.P. and A.G.; visualization, K.S. and A.S. All authors have read and agreed to the published version of the manuscript.

Funding: Anna Sałacińska acknowledges the financial support from an Early Career Grant (grant number EC–45065R–18) from the National Geographic Society, entitled “On the edge of two paleo-continents: in search of the eastern end of the European Variscan orogeny. David Chew acknowledges support from research grant 13/RC/2092 from Science Foundation Ireland, which is co-funded under the European Regional Development Fund and by PIPCO RSG and its member companies.

Acknowledgments: Open access for this publication was paid through funds from internal founding, at INoZ, WNP, UŚ, in Poland.

Conflicts of Interest: The authors declare no conflict of interest.

References

1. Dewey, J.F.; Burke, K. Tibetan, Variscan and Precambrian basement reactivation: Products of continental collision. *J. Geol.* **1973**, *81*, 683–692. [[CrossRef](#)]
2. Hsü, K.J.; Nachev, I.K.; Vuchev, V.T. Geologic evolution of Bulgaria in light of plate tectonics. *Tectonophysics* **1977**, *40*, 245–256. [[CrossRef](#)]
3. Carrigan, C.W.; Mukasa, S.B.; Haydoutov, I.; Kolcheva, K. Age of Variscan magmatism from the Balkan sector of the orogen, central Bulgaria. *Lithos* **2005**, *82*, 125–147. [[CrossRef](#)]
4. Şengör, A.M.C.; Altın, D.; Cin, A.; Ustaömer, T.; Hsü, K.J. *Origin and Assembly of the Tethyside Orogenic Collage at the Expense of Gondwana Land*; Special Publications; Geological Society: London, UK, 1988; Volume 27, pp. 119–181. [[CrossRef](#)]
5. Zanchi, A.; Berra, F.; Mattei, M.; Ghassemi, M.R.; Sabouri, J. Inversion tectonics in central Alborz, Iran. *J. Struct. Geol.* **2006**, *28*, 2023–2037. [[CrossRef](#)]
6. Wilmsen, M.; Fürsich, F.T.; Seyed-Emami, K.; Majidifard, M.R.; Taheri, J. The Cimmerian Orogeny in northern Iran: Tectono-stratigraphic evidence from the foreland. *Terra Nova* **2009**, *21*, 211–218. [[CrossRef](#)]
7. Angiolini, L.; Jadoul, F.; Leng, M.J.; Stephenson, M.H.; Rushton, J.; Chenery, S.; Crippa, G. How cold were the Early Permian glacial tropics? Testing sea-surface temperature using the oxygen isotope composition of rigorously screened brachiopod shells. *J. Geol. Soc.* **2009**, *166*, 933–945. [[CrossRef](#)]
8. Cattò, S.; Cavazza, W.; Zattin, M.; Okay, A.I. No significant Alpine tectonic overprint on the Cimmerian Strandja Massif (SE Bulgaria and NW Turkey). *Int. Geol. Rev.* **2018**, *60*, 513–529. [[CrossRef](#)]
9. Bonev, N.; Filipov, P.; Raicheva, R.; Moritz, R. Timing and tectonic significance of Paleozoic magmatism in the Sakar unit of the Sakar Strandzha Zone, SE Bulgaria. *Int. Geol. Rev.* **2019**, *61*, 1957–1979. [[CrossRef](#)]
10. Gerdjikov, I. Alpine Metamorphism and Granitoid Magmatism in the Strandja Zone: New Data from the Sakar Unit, SE Bulgaria. *Turkish J. Earth Sci.* **2005**, *14*, 167–183.
11. Kamenov, B.K.; Vergilov, V.; Dabovski, C.; Vergilov, I.; Ivchinova, L. The Sakar Batholith: petrology, geochemistry and magmatic evolution. *Geochemistry. Mineral. Petrol.* **2010**, *48*, 1–37.
12. Pristavova, S.; Tzankova, N.; Gospodinov, N.; Filipov, P. Petrological study of metasomatic altered granitoids from Kanarata deposit, Sakar Mountain, southeastern Bulgaria. *J. Min. Geol. Sci.* **2019**, *62*, 53–61.
13. Gerdjikov, I. Transformation of porphyritic granite into banded eye gneiss—An example from the NW margin of Sakar Pluton. *C. R. Acad. Bulg. Sci.* **2003**, *56*, 51–56.
14. Okay, A.I.; Satur, M.; Tüysüz, O.; Akyüz, S.; Chen, F. The tectonics of Strandja Massif: Late-Variscan and mid-Mesozoic deformation and metamorphism in the northern Aegean. *Int. J. Earth Sci.* **2001**, *90*, 217–233. [[CrossRef](#)]
15. Natal'in, B.; Sunal, G.; Gün, E.; Wang, B.; Zhiqing, Y. Precambrian to Early Cretaceous rocks of the Strandja Massif (northwestern Turkey): Evolution of a long lasting magmatic arc. *Can. J. Earth Sci.* **2016**, *53*, 1312–1335. [[CrossRef](#)]
16. Bedi, Y.; Vasilev, E.; Dabovski, C.; Ergen, A.; Okuyucu, C.; Dogan, A.; Kagan Tekin, U.; Ivanova, D.; Boncheva, I.; Lakova, I.; et al. New age data from the tectonostratigraphic units of the Istranca “Massif” in NW Turkey: A correlation with SE Bulgaria. *Geol. Carpath.* **2013**, *64*, 255–277. [[CrossRef](#)]
17. Dabovski, C.; Zagorchev, I. Bulgarian lands in the Alpine tectonic models of the Balkan Peninsula and Eastern Mediterranean region. In *Geology of Bulgaria; Mesozoic*, G., Zagorchev, I., Dabovski, C., Nikolov, T., Eds.; Prof. Marin Drinov Academic Publishing House: Sofia, Bulgaria, 2009; Volume 2, pp. 15–20. (In Bulgarian)
18. Dabovski, C.; Boyanov, I.; Khrishev, K.; Nikolov, T.; Sapounov, L.; Yanev, Y.; Zagorchev, I. Structure and Alpine evolution of Bulgaria. *Geol. Balc.* **2002**, *32*, 9–15.
19. Gerdjikov, I.; Gautier, P.; Cherneva, Z.; Kostopoulos, D. Tectonic setting of ultrahigh-pressure metamorphic rocks from the Chepelare area, Central Rhodope. In Proceedings of the Bulgarian Geological Society Annual Conference, Sofia, Bulgaria, 4–5 November 2003; pp. 44–45.
20. Zagorchev, I. Alpine evolution of the pre-Alpine amphibolites facies basement in south Bulgaria. *Mitt. Österr. Geol. Ges.* **1993**, *86*, 9–23.
21. Lilov, P. Rb-Sr and K-Ar dating of the Sakar granitoid pluton. *Geol. Balc.* **1990**, *20*, 53–60. (In Russian)
22. Skenderov, G.; Skenderova, T. Subduction of the Vardar oceanic crust at the end of Jurassic and its role for the Alpine tectonic-magmatic development of parts of the Balkan Peninsula. *Rev. Bulg. Geol. Soc.* **1995**, *56*, 45–63. (In Russian)

23. Ivanov, Z.; Gerdjikov, I.; Kounov, A. New data and considerations about structure and tectonic evolution of Sakar region, SE Bulgaria. *Annu. Univ. Sofia Geol. Geogr.* **2001**, *91*, 35–80. (In Bulgarian)
24. Palshin, I.; Skenderov, G.; Bojkov, I.; Michailov, Y.; Kotov, E.; Bedrinov, I.; Ivanov, I. New geochronological data for the Cimmeridian and Alpine magmatic and hydrothermal products in the Srednogorie and Stara Planina Zones in Bulgaria. *Rev. Bulg. Geol. Soc.* **1989**, *50*, 75–92. (In Bulgarian)
25. Skenderov, G.; Palshin, I.; Michailov, Y.; Bojkov, I.; Savova, L. On the age of the Sakar granite pluton (South-Eastern Srednogorie). *Geochem. Mineral. Petrol.* **1986**, *22*, 69–81. (In Russian)
26. Boyadjiev, S.; Lilov, P. On the K-Ar dating of the South Bulgarian granitoids from Srednogorie and Sakar-Strandja Zones. Proceedings of the Geological Institute, ser. *Geochem. Mineral. Petrogr.* **1972**, *26*, 121–220. (In Bulgarian)
27. Firsov, L. On the age of South-Bulgarian granites in the Rhodopes, Srednogorie and Sakar-Strandja areas. *Geol. Geophys.* **1975**, *1*, 27–34. (In Russian)
28. Peytcheva, I.; Georgiev, S.; von Quadt, A. U/Pb ID-TIMS dating of zircons from the Sakar-Strandzha Zone: New data and old questions about the Variscan orogeny in SE Europe. In Proceedings of the Annual Conference of the Bulgaria Geological Society “Geosciences 2016”, Sofia, Bulgaria, 7–8 December 2016; Bulgarian Geological Society: Sofia, Bulgaria, 2016; pp. 71–72.
29. Zagorchev, I.; Lilov, P.; Moorbath, S. Results of the Rubidium-Strontium and Potassium-Argon radiogeochronological studies on the metamorphic and magmatic rocks in South Bulgaria. *Geol. Balc.* **1989**, *19*, 41–54.
30. Dencheva, S. Apatite from Sakar Mountain, Bulgaria—Morphology and physical properties. In Proceedings of the National Conference with International Participation “Geosciences 2017”, Sofia, Bulgaria, 7–8 December 2017; Bulgarian Geological Society: Sofia, Bulgaria, 2017; pp. 21–22.
31. Chew, D.M.; Petrus, J.A.; Kamber, B.S. U-Pb LA-ICPMS dating using accessory mineral standards with variable common Pb. *Chem. Geol.* **2014**, *363*, 185–199. [[CrossRef](#)]
32. Petrus, J.A.; Kamber, B.S. VizualAge: A Novel Approach to Laser Ablation ICP-MS U-Pb Geochronology Data Reduction. *Geostand. Geoanalytical Res.* **2012**, *36*, 247–270. [[CrossRef](#)]
33. Paton, C.; Helstrom, J.; Paul, B.; Woodhead, J.; Herqt, J. Iolite: Freeware for the visualisation and processing of mass spectrometric data. *J. Anal. At. Spectrom.* **2011**, *26*, 2508–2518. [[CrossRef](#)]
34. Thomson, S.N.; Gehrels, G.E.; Ruiz, J.; Buchwaldt, R. Routine low-damage apatite U–Pb dating using laser ablation-multicollector-ICPMS. *Geochem. Geophys. Geosyst.* **2012**, *13*, Q0AA21. [[CrossRef](#)]
35. Schoene, B.; Bowring, S.A. U–Pb systematics of the McClure Mountain syenite: Thermochronological constraints on the age of the Ar-40/Ar-39 standard MMhb. *Contrib. Mineral. Petrol.* **2006**, *151*, 615–630. [[CrossRef](#)]
36. McDowell, F.W.; McIntosh, W.C.; Farley, K.A. A precise ^{40}Ar - ^{39}Ar reference age for the Durango apatite (U-Th)/He and fission-track dating standard. *Chem. Geol.* **2005**, *214*, 249–263. [[CrossRef](#)]
37. Stacey, J.S.; Kramers, J.D. Approximation of terrestrial lead isotope evolution by a two-stage model. *Earth Planet. Sci. Lett.* **1975**, *26*, 207–221. [[CrossRef](#)]
38. Spandler, C.; Hammerli, J.; Sha, P.; Hilbert-Wolf, H.; Hu, Y.; Roberts, E.; Schmitz, M. MKED1: A new titanite standard for in situ analysis of Sm–Nd isotopes and U–Pb geochronology. *Chem. Geol.* **2016**, *425*, 110–126. [[CrossRef](#)]
39. Kennedy, A.K.; Kamo, S.L.; Nasdala, L.; Timms, N.E. Grenville skarn titanite: Potential reference material for SIMS U–Th–Pb analysis. *Can. Mineral.* **2010**, *48*, 1423–1443. [[CrossRef](#)]
40. Aleinikoff, J.N.; Wintsch, R.; Tollo, R.P.; Unruh, D.M.; Fanning, C.M.; Schmitz, M.D. Ages and origins of rocks of the Killingworth dome, south-central Connecticut: Implications for the tectonic evolution of southern New England. *Am. J. Sci.* **2007**, *307*, 63–118. [[CrossRef](#)]
41. Bailey, S.W. *Structures of Layer Silicates: In Crystal Structures of Clay Minerals and Their X-Ray Identification*; Brindley, G.W., Brown, G., Eds.; Mineralogical Society: London, UK, 1980; pp. 1–123.
42. Cathelineau, M.; Nieva, D. A chlorite solid solution geothermometer. The Los Azufres (Mexico) geothermal system. *Contrib. Mineral. Petrol.* **1985**, *91*, 235–244. [[CrossRef](#)]
43. Jowett, E. Fitting iron and magnesium into the hydrothermal chlorite geothermometer. In Abstract Book. In Proceedings of the GAC/MAC/SEG Joint Annual Meeting, Toronto, ON, Canada, 27–29 May 1991; Volume 16, p. A62.

44. Kranidiotis, P.; MacLean, W.H. Systematics of chlorite alteration at the Phelps Dodge massive sulfide deposit, Matagami, Quebec. *Econ. Geol.* **1987**, *82*, 1898–1911. [[CrossRef](#)]
45. Tilton, G.R.; Grünenfelder, M. Sphene: Uranium-lead ages. *Science* **1968**, *159*, 1458–1461. [[CrossRef](#)]
46. Tucker, R.D.; Raheim, A.; Krogh, T.E.; Corfu, F. Uranium-lead zircon and titanite ages from the northern portion of the Western Gneiss region, south-central Norway. *EPSL* **1987**, *81*, 203–211. [[CrossRef](#)]
47. Heaman, L.; Parrish, R. U-Pb geochronology of accessory minerals. In *Applications of Radiometric Isotope Systems to Problems in Geology*; Heaman, L., Ludden, J.N., Eds.; Mineralogical Association of Canada: Quebec, QC, Canada, 1991; Volume 19, pp. 59–102.
48. Scott, D.J.; St-Onge, M.R. Constraints on Pb closure temperature in titanite based on rocks from the Ungava orogen, Canada: Implications for U-Pb geochronology and P-T-t path determinations. *Geology* **1995**, *23*, 1123–1126. [[CrossRef](#)]
49. Watson, E.B.; Harrison, T.M.; Ryerson, F.J. Diffusion of Sm, Sr and Pb in fluoroapatite. *Geochim. Cosmochim. Acta* **1985**, *49*, 1813–1823. [[CrossRef](#)]
50. Chemiak, D.J.; Lanford, W.A.; Ryerson, F.J. Lead diffusion in apatite and zircon using ion implantation and Rutherford backscattering techniques. *Geochim. Cosmochim. Acta* **1991**, *55*, 1663–1674.
51. Chamberlain, K.R.; Bowring, S.A. Apatite–feldspar U–Pb thermochronometer: A reliable, mid-range (~450 °C), diffusion-controlled system. *Chem. Geol.* **2000**, *172*, 173–200. [[CrossRef](#)]
52. Stalder, H.A. Petrographische und mineralogische Untersuchungen im Grimselgebiet (Mittleres Aarmassiv). *Schweiz. Min. Alogischen Petrogr. Mitt.* **1964**, *44*, 187–398.
53. Schmid, S.M.; Fügenschuh, B.; Kissling, E.; Schuster, R. Tectonic map and overall architecture of the Alpine orogen. *Eclogae Geol. Helv.* **2004**, *97*, 93–117. [[CrossRef](#)]
54. Mullis, J. Fluid inclusion studies during very low-grade metamorphism. In *Low Temperature Metamorphism*; Frey, M., Ed.; Blackie: London, UK, 1988; pp. 162–199.
55. Mullis, J.; Dubessy, J.; Poty, B.; O’Neil, J. Fluid regimes during late stages of a continental collision: Physical, chemical, and stable isotope measurements of fluid inclusions in fissure quartz from a geotraverse through the Central Alps, Switzerland. *Geochim. Cosmochim. Acta.* **1994**, *58*, 2239–2267. [[CrossRef](#)]
56. Taylor, R.P.; Fryer, B.J. Multiple-stage hydrothermal alteration in porphyry copper systems in northern Turkey: The temporal interplay of potassic, propylitic, and phyllic fluids. *Can. J. Earth. Sci.* **1980**, *17*, 901–926. [[CrossRef](#)]
57. Elmas, A.; Yilmaz, I.; Yigitbas, E.; Ullrich, T. A Late Jurassic–Early Cretaceous metamorphic core complex, Strandja Massif, NW Turkey. *Int. J. Earth Sci.* **2011**, *100*, 1251–1263. [[CrossRef](#)]
58. Stampfli, G.; Kozur, H. Europe from Variscan to the Alpine cycles. In *European Lithosphere Dynamics*, 32th ed.; Geological Society of London: London, UK, 2006; Volume 32, pp. 57–82.
59. Stampfli, G.; Mosar, J.; Favre, P.; Pillevert, A.; Vannay, J.-C. Permo-Mesozoic evolution of the western Tethyan realm: The Neotethys/EastMediterranean connection. In *PeriTethys Memoir 6: Peritethyan Rift/Wrench Basins and Passive Margins*; Mémoires du Muséum National d’Histoire; Ziegler, P., Cavazza, W., Robertson, A., Crasquinsoleau, S., Eds.; IGCP 369: Lisbon, Portugal, 2001; Volume 186, pp. 51–108.
60. Golonka, J.; Krobicki, M.; Oszczytko, N.; Ślaczka, A.; Słomka, T. Geodynamic evolution and palaeogeography of the Polish Carpathians and adjacent areas during Neo-Cimmerian and preceding events (latest Triassic-earliest cretaceous). *Geol. Soc. Spec. Publ.* **2003**, *208*, 138–158. [[CrossRef](#)]
61. Szopa, K.; Włodyka, R.; Chew, D. LA-ICP-MS U-Pb apatite dating of Lower Cretaceous rocks from teschenite-picrite association in the Silesian Unit (southern Poland). *Geol. Carpathica* **2014**, *65*, 273–284. [[CrossRef](#)]
62. Gawęda, A.; Szopa, K.; Chew, D.; O’Sullivan, G.J.; Burda, J.; Klötzli, U.; Golonka, J. Variscan post-collisional cooling and uplift of the Tatra Mountains crystalline block constrained by integrated zircon, apatite and titanite LA-(MC)-ICP-MS U-Pb dating and rare earth element analyses. *Chem. Geol.* **2018**, *484*, 191–209. [[CrossRef](#)]
63. Ballato, P.; Nowaczyk, N.R.; Landgraf, A.; Strecker, M.R.; Friedrich, A.; Tabatabaei, S.H. Tectonic control on sedimentary facies pattern and sediment accumulation rates in the Miocene foreland basin of the southern Alborz mountains, northern Iran. *Tectonics* **2008**, *27*, TC6001. [[CrossRef](#)]
64. Şengör, A.M.C. Mid-Mesozoic closure of Permo-Triassic Tethys and its implications. *Nature* **1979**, *279*, 590–593. [[CrossRef](#)]

65. Stampfli, G.; Borel, G. The TRANSMED transects in space and time: Constraints on the Paleotectonic evolution of the Mediterranean Domain. In *The TRANSMED Atlas: The Mediterranean Region from Crust to Mantle*; Cavazza, W., Roure, F., Spakman, W., Ziegler, P., Eds.; Springer: Berlin, Germany, 2004; pp. 53–80.
66. Stampfli, G.; Hochard, C. Plate tectonics of the Alpine realm. Geol. Soc. London. In *Ancient Orogens and Modern Analogues*; Special Publications; The Geological Society of London: London, UK, 2009; Volume 327, pp. 89–111.
67. Okay, A.I.; Sunal, G.; Sherlock, S.; Altiner, D.; Tüysüz, O.; Kylander-Clark, A.R.C.; Aygül, M. Early Cretaceous sedimentation and orogeny on the southern active margin of Eurasia: Central Pontides, Turkey. *Tectonics* **2013**, *32*, 1247–1271. [[CrossRef](#)]
68. Okay, A.I.; Altiner, D.; Kiliç, A.M. Triassic limestone, turbidites and serpentinite—the Cimmeride orogeny in the Central Pontides. *Geol. Mag.* **2015**, *152*, 460–479. [[CrossRef](#)]
69. Topuz, G.; Göçmengil, G.; Rolland, Y.; Çelic, Ö.F.; Zack, T.; Schmitt, A.K. Jurassic accretionary complex and ophiolite from northeast Turkey: No evidence for the Cimmerian continental ribbon. *Geology* **2013**, *41*, 255–258. [[CrossRef](#)]
70. Hrubcová, P.; Šroda, P.; Grad, M.; Geissler, W.H.; Guterch, A.; Vozár, J.; Hegedűs, E. From the Variscan to the Alpine Orogeny: Crustal structure of the Bohemian Massif and the Western Carpathians in the light of the SUDETES 2003 seismic data 2010. *Geophys. J. Int.* **2010**, *183*, 611–633. [[CrossRef](#)]
71. Georgiev, S.; von Quadt, A.; Heinrich, C.A.; Peytcheva, I.; Marchev, P. Time evolution of a rifted continental arc: Integrated ID-TIMS and LA-ICPMS study of magmatic zircons from the Eastern Srednogorie, Bulgaria. *Lithos* **2012**, *154*, 53–67. [[CrossRef](#)]
72. Lips, A.; White, S.; Wijbrans, J. Middle-Late Alpine thermotectonic evolution of the southern Rhodope Massif, Greece. *Geodin. Acta* **2000**, *13*, 281–292. [[CrossRef](#)]



© 2020 by the authors. Licensee MDPI, Basel, Switzerland. This article is an open access article distributed under the terms and conditions of the Creative Commons Attribution (CC BY) license (<http://creativecommons.org/licenses/by/4.0/>).